



Aerodynamic Characterization of Bullet Heads with Different Arcuate Curves

B. Hao^{1,2,3}, Q. Jiang^{2†}, C. Xu² and L. Liu²

¹*School of Mechanical Engineering and Automation, Northeastern University, Shenyang110819, China*

²*School of Control Engineering, Northeastern University at Qinhuangdao, Qinhuangdao066004, China*

³*Key Laboratory of Vibration and Control of Aeronautical Power Equipment of Ministry of Education, Shenyang110819, China*

†Corresponding Author Email: 2201979@stu.neu.edu.cn

ABSTRACT

The bullet shape is critical in efficient bullet design because it affects the lift and drag forces. This paper proposes a new bullet shape with a logarithmic curve and analyzes the lift and drag coefficients of bullets with different curves under different angles of attack. The results are compared with a bullet whose shape is described by the power law curve. Fluent simulations demonstrate that the optimal power exponent values are 0.65, 0.6, and 0.65 for the bullet with the power law curve and 1.3, 1, and 1 for the bullet with the logarithmic curve at 0°, 30°, and 40° angles of attack, respectively. At a 0° angle of attack, the lift coefficient of the logarithmic curve is the largest. The lift force of the bullet with the logarithmic curve is 129.4% higher than that with the von Karman curve. The drag coefficient is the largest for the bullet with the rectilinear curve; it is 1.30% larger than that of the bullet with the logarithmic curve. At 30° and 40° angles of attack, the lift coefficient of the bullet with the power law curve is larger. The difference in the lift coefficients between the two angles of attack is 18.47%. The bullet's drag coefficient is the largest for the logarithmic curve, and the difference in the drag coefficients between the two angles of attack is 18.59%.

Article History

Received September 22, 2023

Revised December 14, 2023

Accepted December 16, 2023

Available online February 24, 2024

Keywords:

Arcuate Curve

Drag Coefficient

Lift Coefficient

Power exponent

Computational Fluid Dynamics

1. INTRODUCTION

Bullets are used extensively in modern warfare (Rhee et al., 2016; Bateman & Force 2022). The bullet's shape and size affect its aerodynamic characteristics, flight stability, and firing power (Shi et al., 2017). The shape of the bullet arc curve affects the bullet's aerodynamic characteristics, and the flight velocity is related to the flight resistance. The resistance, lift, and arcuate curve must be considered in the design of the bullet parameters (Rahman 2020).

Numerous researchers have investigated bullet design. McCoy (1999) and Davis et al. (2009) conducted systematic experimental analyses on the properties of existing projectiles. References (Silton, 2005; Silton & Weinacht, 2008; Doig et al., 2010) investigated the flow field using computational fluid dynamics. In addition, many experts and scholars analyzed the shape of projectiles from multiple perspectives, including a finite range (Sadowski et al., 1984), manufacturing quality (Silva et al., 2011), and flow control (Ma et al., 2016).

Abdullah et al. (2022) investigated the effect of the angle of attack and projectile size on the lift and resistance and observed a significant increase in the lift and resistance with increases in the bullet's length and angle of attack.

In this paper examines the effect of the warhead's shape on its lift and drag coefficients at various angles of attack (0, 30, and 40 degrees). The optimal power exponent (n) value of newly designed warheads with a logarithmic curve is determined, and the lift and drag coefficients of existing and newly designed warheads are compared. Equation-driven curves are modeled using SolidWorks, and the characteristics of different warheads are simulated using Fluent.

The innovations of this study are as follows: (a) A new warhead with a shape described by a logarithmic curve is designed. (b) The optimal power exponents for warhead shapes described by the power law and logarithmic curves are determined for different attack angles. The lift and drag force of warheads with different exponents is discussed. (c) The lift and drag coefficients

NOMENCLATURE			
R_d	maximum radius of arcuate curves	L	theoretical length of curves
n	power exponent	ω_k	angular velocity
F_x	vertical component	F_y	horizontal component
a	angle of attack	F	total force
C_L	lift coefficient	C_D	drag coefficient
S_1, S_2	maximum cross-sectional area of the projectile	ρ_l	air density
u	projectile velocity	μ_t	turbulent viscosity
u_i	time-averaged velocity	k_β	turbulence energy
μ	hydrodynamic viscosity	C_a	empirical function
C_b	empirical function	G	turbulent energy
\mathcal{E}_x	turbulence dissipation rate	σ_1	Prandtl number
σ_2	Prandtl number	E	fluid energy
C_μ	variable in the turbulent viscosity equation	$\overline{\Omega}_{ij}$	time-averaged rotation tensor

of warheads with different arcuate curves and different attack angles are compared.

2. EXPERIMENTAL AND NUMERICAL FRAMEWORKS

2.1 Existing and Proposed Warheads

This study considers warhead shapes described by four arcuate curves, as shown in Fig. 1. In the y - x coordinate system, the x -axis indicates the direction from the bottom to the tip of the bullet, and the y -axis corresponds to the radius of the warhead. The four curves include the rectilinear curve, power law curve, von Karman curve, and the proposed logarithmic curve. The equations describing the power law, von Karman, and logarithmic curves are as follows:

1. Power law curve:

$$y = R_d \left(\frac{x}{L} \right)^n \quad (1)$$

2. Von Karman curve:

$$y = \frac{R_d}{\sqrt{\pi}} \left(\theta - \frac{1}{2} \sin 2\theta \right), \theta = \arccos \left(1 - 2 \frac{x}{L} \right) \quad (2)$$

3. Logarithmic curve:

$$y = \frac{R_d}{\ln(L-1)} \cdot \ln(L+1-x)^n \quad (3)$$

where R_d is the maximum radius of the arcuate curve, L is the theoretical length of the curve section, n is the power exponent of the curve. For the power law curve, n generally ranges from 0.6 to 0.75, and the optimal n of the Logarithmic curve ranges from 1.2 to 1.5.

The different shapes must have the same theoretical aspect ratio to enable comparisons. Therefore, we used the same radius of circle for the leading-edge passivation to ensure that different warheads had the same tail size and tip size. The curve after frontal passivation is shown in Fig. 1. However, due to the curvature change of different curves, the length and slenderness ratio of the curves differed due to different curvatures.

Figure 2(a) and (b) respectively show the power law and logarithmic bullets with various power exponents.

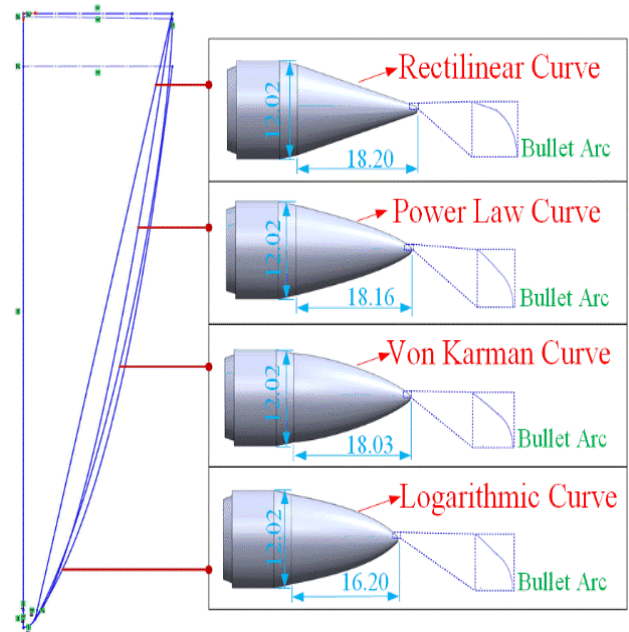


Fig. 1 Different shapes of warhead nose cones

2.2 Numerical Methods and Mathematical Models

We briefly describe the mathematical equations and principles required to calculate the drag and lift indices. The components of force on the warhead include horizontal and vertical forces:

$$F_y = F \sin(a) \quad (4)$$

$$F_x = F \cos(a) \quad (5)$$

where F is the total strength on the warhead, and a is the angle between the warhead and the horizontal plane. The following equations define the lifting coefficient and the drag coefficient (C_L and C_D):

$$C_L = \frac{F_y}{S_1 \frac{\rho_l u^2}{2}} \quad (6)$$

$$C_D = \frac{F_x}{S_2 \frac{\rho_l u^2}{2}} \quad (7)$$

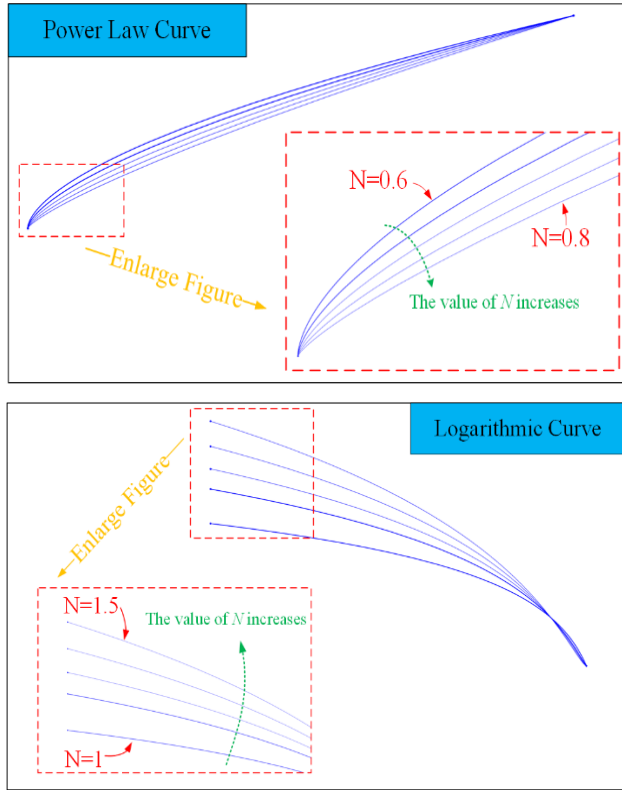


Fig. 2 Power law (a) and logarithmic (b) curves with different power exponents

where S_1 and S_2 denote the maximum cross-sectional area of the projectile (S_1 and S_2 represent constants). ρ_1 denotes air density, and u is the speed of the projectile.

The relevant equations for *realizable* k - \mathcal{E} turbulence model are used to simulate the warhead's aerodynamic characteristics and predict the wall flow and free shear flow. The relevant equations for k and \mathcal{E} in the *realizable* k - \mathcal{E} turbulence model are as follows (Shih et al. 1995; Qian et al. 2009):

$$\frac{\partial(\rho_1 k_\beta)}{\partial t} + \frac{\partial(\rho_1 k_\beta u_i)}{\partial x_i} = \frac{\partial}{\partial x_j} \left[\left(\mu + \frac{\mu_t}{\sigma_1} \right) \frac{\partial k_\beta}{\partial x_j} \right] + G - \rho_1 \mathcal{E}_x \quad (8)$$

$$\frac{\partial(\rho_1 \mathcal{E}_x)}{\partial t} + \frac{\partial(\rho_1 \mathcal{E}_x u_i)}{\partial x_i} = \frac{\partial}{\partial x_j} \left[\left(\mu + \frac{\mu_t}{\sigma_2} \right) \frac{\partial \mathcal{E}_x}{\partial x_j} \right] + \rho_1 C_a S \mathcal{E}_x - \rho_1 C_b \frac{\mathcal{E}_x^2}{k_\beta + \sqrt{\nu \mathcal{E}_x}} \quad (9)$$

In Eq. (9),

$$\mu_t = \rho_1 C_\mu \frac{k_\beta^2}{\mathcal{E}_x} \quad (10)$$

$$C_\mu = \frac{1}{A_0 + A_w U^* k_\beta / \mathcal{E}_x} \quad (11)$$

Then,

$$\left\{ \begin{array}{l} \sigma_1 = 1, \sigma_2 = 1.2, C_b = 1.9 \\ C_a = \max \left(0.43, \frac{\eta}{\eta + 5} \right) \\ \eta = (2E_{ij} \cdot E_{ij})^{\frac{1}{2}} \frac{k_\beta}{\mathcal{E}_x} \\ S = \sqrt{2S_{ij}S_{ij}} \\ S_{ij} = \frac{1}{2} \left(\frac{\partial u_i}{\partial x_j} + \frac{\partial u_j}{\partial x_i} \right) \\ G = \mu_t \left(\frac{\partial u_i}{\partial x_j} + \frac{\partial u_j}{\partial x_i} \right) \frac{\partial u_i}{\partial x_j} \end{array} \right. \quad (12)$$

Then,

$$\left\{ \begin{array}{l} A_0 = 4, A_w = \sqrt{6} \cos \varphi_1 \\ \varphi_1 = \frac{1}{3} \cos^{-1} \left(\sqrt{6} W_\kappa \right) \\ W_\kappa = \frac{E_{ij} E_{jk} E_{kj}}{(E_{ij} E_{ij})^{1/2}} \\ E_{ij} = \frac{1}{2} \left(\frac{\partial u_i}{\partial x_j} + \frac{\partial u_j}{\partial x_i} \right) \\ U^* = \sqrt{E_{ij} E_{ij} + \Omega_{ij}^* \Omega_{ij}^*} \\ \Omega_{ij}^* = \Omega_{ij} - 2\mathcal{E}'_{ijk} \omega_k, \Omega_{ij} = \overline{\Omega_{ij}} - \mathcal{E}'_{ijk} \omega_k \end{array} \right. \quad (13)$$

where μ_t denotes the turbulent viscosity. u_i is the time-averaged velocity. k_β is the turbulence energy. μ denotes represents the hydrodynamic viscosity. C_a and C_b are the empirical functions. G denotes the turbulent energy due to the average velocity. The turbulent dissipation rate is denoted by \mathcal{E}_x . The Prandtl numbers corresponding to the turbulent kinetic energy k_β and the turbulent dissipation rate \mathcal{E}_x is represented by σ_1 and σ_2 , respectively. E denotes the fluid energy. v represents the component of the velocity vector in the z -axis direction. C_μ is a variable in the turbulent viscosity equation, it is used to stratify certain mathematical constraints of the Reynolds stress. $\overline{\Omega_{ij}}$ is the time-averaged rotation rate tensor from the reference system of the angular speed ω_k .

2.3 Experiment and Simulation

This paper analyzes the influence of different arcuate curves on the lift and drag coefficients, especially the projectile's aerodynamic characteristics.

The experimental warhead consists of the tip, body, and tail. The maximum diameter of the warhead is $D_m = 12.02$ mm, the theoretical length is $L = 30$ mm, and the tip is an arc curve with a radius of 0.51(mm). The same tip size ($l = 0.88$ mm) was used for different warhead shapes to ensure comparability (Fig. 3).

The calculation domain of warhead's movement in the air is shown in Fig. 4. A 2L air domain was used at the warhead's front, and a 10L air domain was used at the warhead's rear in the x -axis. 5L air domains were used in the y - and z -axes of the warhead to prevent border influences. The entrance of the calculation domain was the velocity inlet, the exit was the pressure outlet, and the other borders were walls. The warhead's attack angle was

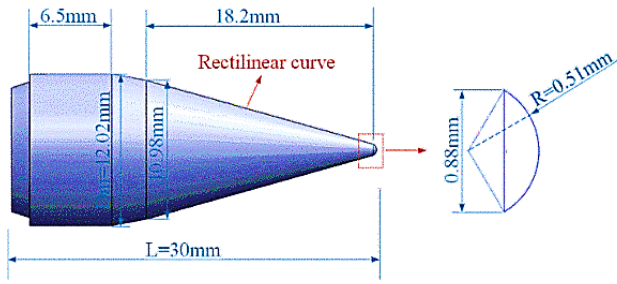


Fig. 3 Dimensions of the bullet with a rectilinear curve

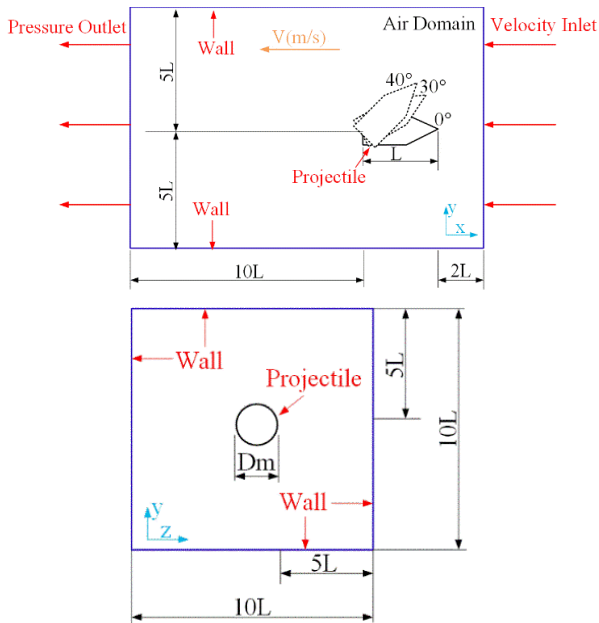


Fig. 4 Air domain of the bullet's motion

0°, 30°, and 40°. The air flowed in the negative x-axis direction.

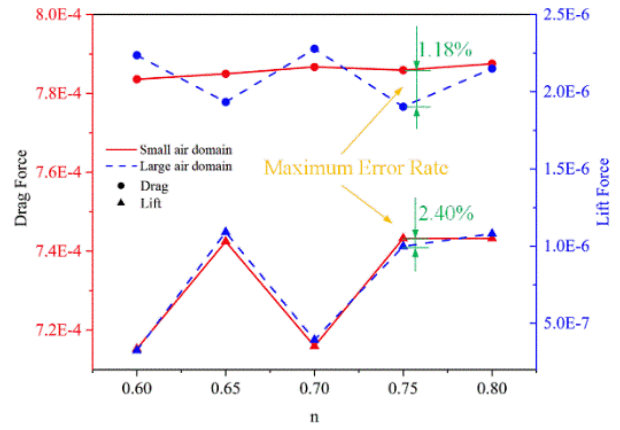
This paper simulates low-speed wind tunnel tests. The steady-state method was used to solve the problem. A density-based solver was selected, and an enhanced wall function (EWF) was used. A second-order upwind format was used for spatial discretization, and the velocity at the entrance was 5.2 m/s. Compressible flow was used.

The impact of the calculation domain size on the simulation values was analyzed. The lift and drag forces of the bullet with the power law curve in the larger (4L × 15L × 7.5L) and the smaller (2L × 10L × 5L) calculation domains are shown in Fig. 5.

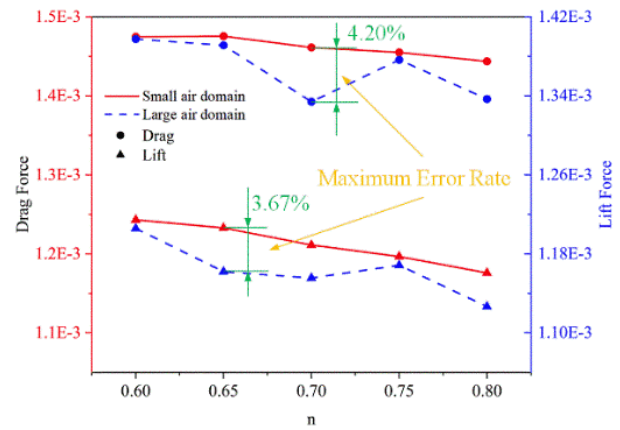
The values show that the error rate is small for different attack angles, with a maximum error rate of 4.30%. Therefore, the size of the computing domain does not affect the simulation results. We used the smaller computing domain to reduce the calculation time.

2.4 Grid Generation

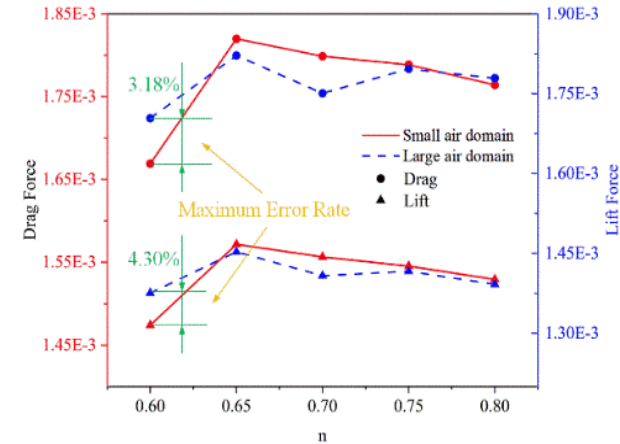
The mesh size has a substantial influence on the numerical simulation results, and the correct mesh size



(a) 0° angle of attack



(b) 30° angle of attack



(c) 40° angle of attack

Fig. 5 Comparison of two computing domains

results in higher accuracy. The geometry of the object should be accurately represented.

Figure 6 shows the mesh size of the calculation domain during the warhead's movement in the air. The calculation domain near the warhead has higher mesh density, whereas the rest has lower density to ensure sufficient calculation accuracy and low computational complexity.

A grid independence test was conducted (Fig. 7). The lift and drag coefficients exhibit negligible change when the number of elements exceeds 3.3 million. Therefore, this grid size was used to obtain accurate simulation results.

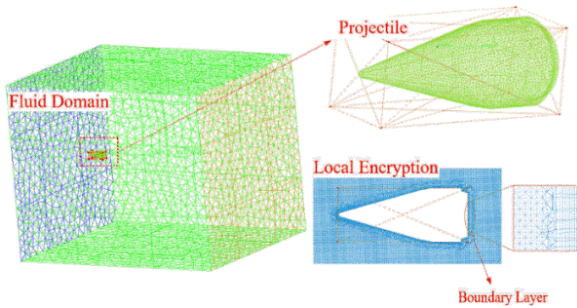


Fig. 6 Schematic diagram of the grid

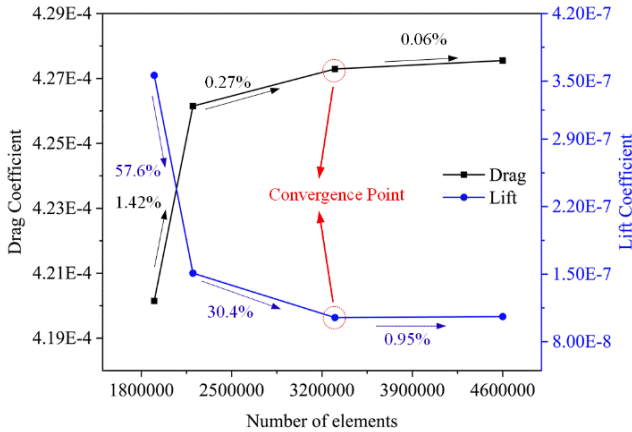


Fig. 7 Grid independence verification

Table 1 Comparison of simulation results

	First simulation	Second simulation	Third simulation
Small Air Domain	2.966E-4	2.969E-4	2.973E-4
Large Air Domain	3.088E-4	3.085E-4	3.090E-4

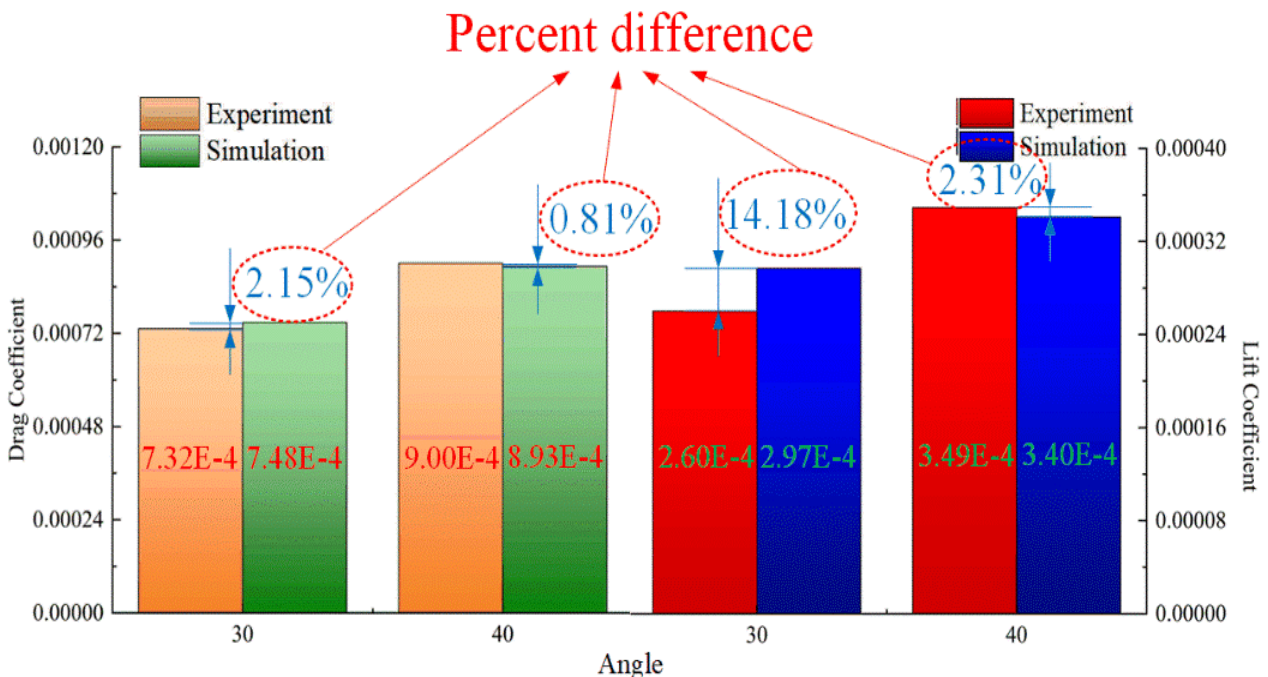


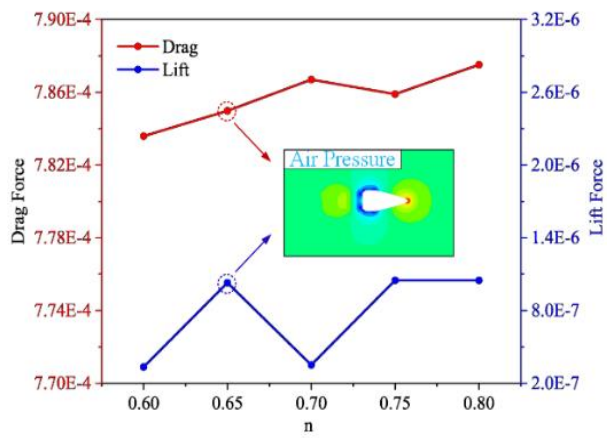
Fig. 8 Comparison between simulation and experimental results

2.5 Numerical Verification

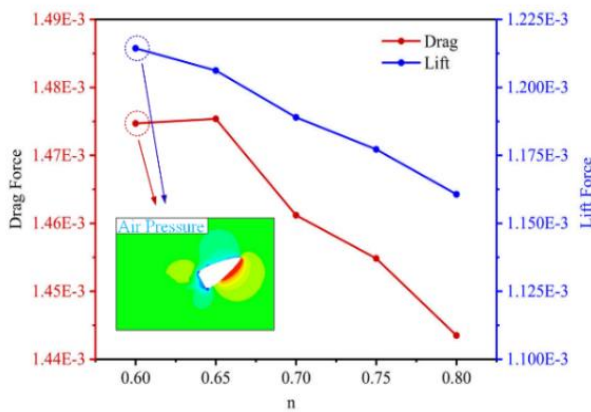
The warhead characterized by the rectilinear curve was selected for the simulation (Fig. 3). The inlet velocity was 5.2 m/s, and the angle of attack was 30° and 40° for the numerical verification. Comparison of simulated results with experimental data in the literature (Abdullah et al., 2022) (Fig. 8). At a 30° (40°) angle of attack, the error rates are 2.15% (0.81%) and 14.18% (2.31%) for the drag and lift coefficients, respectively. The average error rates are 8.25% for the lift coefficient and 1.48% for the drag coefficient.

The error rate is larger for the 30° angle of attack and for the comparison with the experimental results in Reference (Abdullah et al., 2022). In order to avoid large error rates due to calculation domain size and calculation contingency. We repeated the simulation three times for the small and large domains (Table 1).

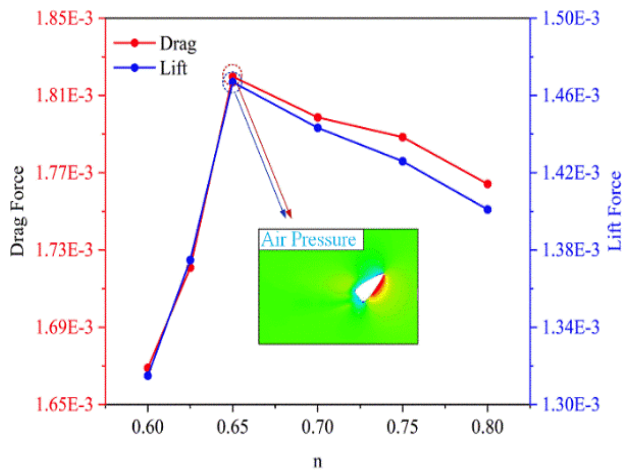
The simulation results show that there are little differences among the three simulations, and the average simulation values are 2.969E-4 and 3.088E-4 for the two domains, respectively. The overall error rate of the two air domains is less than 4%, and the average error rate is 3.84%. Therefore, the simulation results are considered reliable given that several errors can occur in the experiment, including wind speed error, calculation error, and experimental conditions.



(a) 0° angle of attack



(b) 30° angle of attack



(c) 40° angle of attack

Fig. 9 Bullet’s drag and lift forces for the power law curve

3. RESULTS AND DISCUSSION

3.1 Curve Optimization

3.1.1 Power Law Curve

The power exponent n substantially affects the power law curve (Eq. (1)). n typically ranges from 0.6 to 0.8. We used 5 values of n with an increment of 0.05 to determine the optimal value of n . $n=0.625$ was used in the simulation for an angle of attack of 40° to achieve a smoother curve.

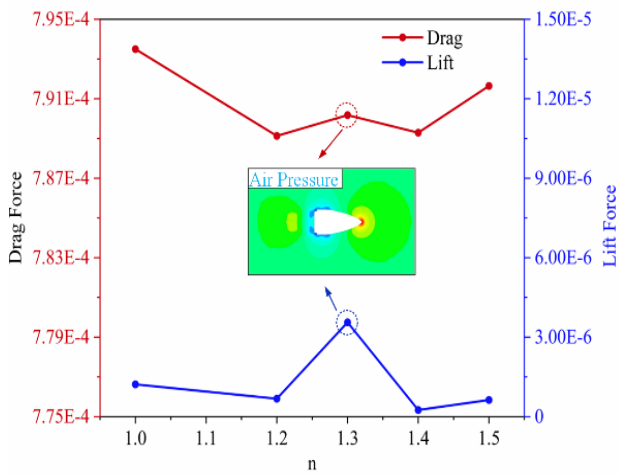
The lift and drag forces are compared in Fig. 9(a), (b), and (c) for 0°, 30°, and 40° angles of attack, respectively.

As the power exponent increases, the drag and lift forces increase, decrease, and increase at a 0° angle of attack. The lift force reaches the maximum when n is 0.65, and the resistance of the warhead is relatively small. The optimal value of the power exponent is 0.65. The trends of the lift and drag forces are different for a 30° angle of attack (Fig. 9(b)). As n increases, the drag force increases and decreases, whereas the lift force shows a decreasing trend. The optimal value of the power exponent is 0.6, when the difference between the drag and lift forces is the smallest. The lift and drag forces exhibit the same trend at a 40° angle of attack (Fig. 9(c)). As n increases, both forces increase and decrease. The difference between the lift and drag forces is the smallest when n is 0.65, and the lift force reaches the maximum.

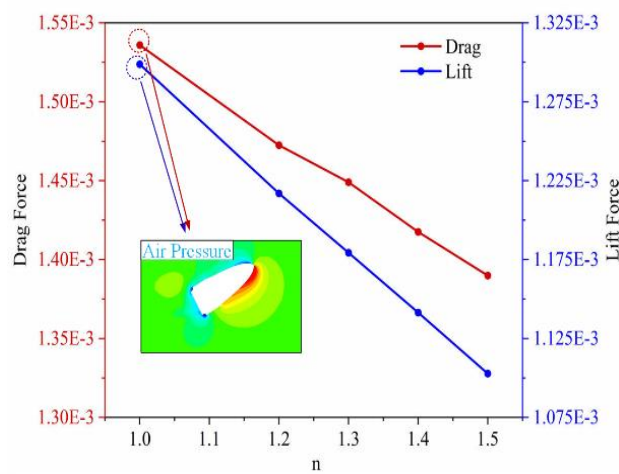
The air stress at the tip of the warhead is large, and a low-pressure area occurs at the tail. The vertical component of air pressure acting on the warhead is the lift force, and horizontal component of the force causes the resistance of the warhead. At a 0° angle of attack, the main force direction occurs at the tip along the axis; therefore, the drag force is much greater than the lift force (Shinde et al., 2023). The inclination angle has a large influence on the forces acting on the warhead. The inclination angle differs for different n values. The passivation degree has the largest influence on the warhead’s resistance at a 30° angle of attack. As the power exponent increases, the passivation degree decreases, and the resistance of the projectile decreases. At a 40° angle of attack, the warhead’s resistance is primarily affected by the airflow at the top of the warhead at n values from 0.6 to 0.65. As the power index grows, the reaction force of the airflow and the warhead’s resistance increase. The passivation degree and the resistance decrease when the power exponent exceeds 0.65. As the angle of attack grows, the stress area of the warhead increases. As shown in Fig. 9(b), the air pressure is the largest on the lower side of the warhead and is relatively small on the upper side. As the stress area on the tail increases, the force acting on the warhead increases, and the lift force increases significantly and is much higher compared to the 0° angle of attack. As displayed in Fig. 9(c), the lower area of the warhead and the tail area are the main stress areas. The average lift force and average resistance are 18.2% and 14.6% higher at a 40° than at a 30° angle of attack.

3.1.2 Logarithmic Curve

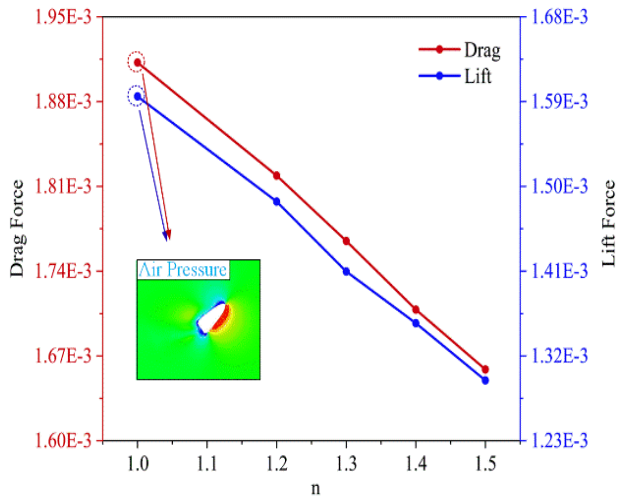
The simulation results for the bullet’s drag and lift forces for the logarithmic curve are shown in Fig. 10. The trends of the lift and drag forces are the same for a 0° angle of attack (Fig. 10(a)). The lift force is the largest when $n=1.3$. The resistance is relatively low, and the difference between the lift force and drag force is the smallest. The optimal value of n is 1.3. The lift and drag forces show the same decreasing trend at 30° and 40° angles of attack (Fig. 10(b) and (c)). The optimal power exponent value is 1 when the difference between the lift and drag forces is the smallest, and the lift force reaches the maximum under the same conditions. At 30° and 40° angles of attack, the higher the degree of warhead passivation, the greater the



(a) 0° angle of attack



(b) 30° angle of attack



(c) 40° angle of attack

Fig. 10 Bullet’s drag and lift forces for the logarithmic curve

turbulent flow at the tip of the warhead and the greater the drag force. As the power exponent increases, the passivation degree and the resistance of the warhead decrease.

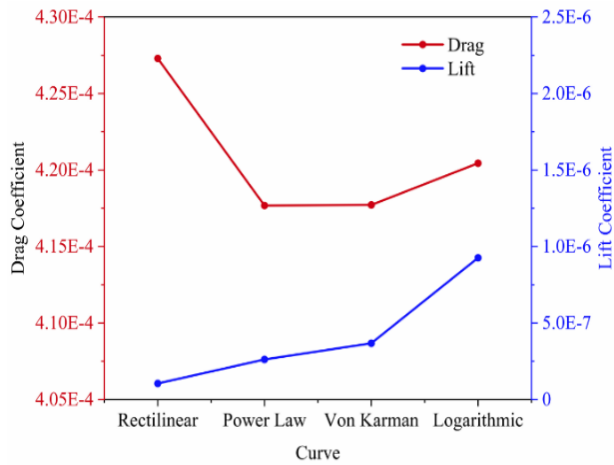
The air pressure near the warhead is similar for the logarithmic curve and the power law curve. As the angle of attack grows, the stressed area of the warhead increases, and lift force increases significantly. The low-pressure area occurs near the warhead’s tail and the sharp corner on the upper side, and the air pressure is relatively large below the warhead’s nose. According to Bernoulli’s principle, a low-pressure area occurs since the air velocity increases quickly at the sharp corner and the tail of the warhead. Due to a thin air layer on the upper side of the warhead, the air density drops sharply, causing a low-pressure area on the warhead’s upper side. The air pressure increases toward the warheads’ tip, forming a high-pressure zone under the tip. As the angle of attack increases, the high-stress zone and the force acting on the warhead increase. Therefore, the lift and drag forces increase (Eqs. (6) and (7)). The air pressure near the warhead is uniform at a 0° angle of attack and symmetrical around the x-axis. The air pressure is much lower on the warhead’s side than at the tip. According to Newton’s third law, the lift force is significantly lower than the resistance.

3.2 Comparison of Bullets Described by Different Curves

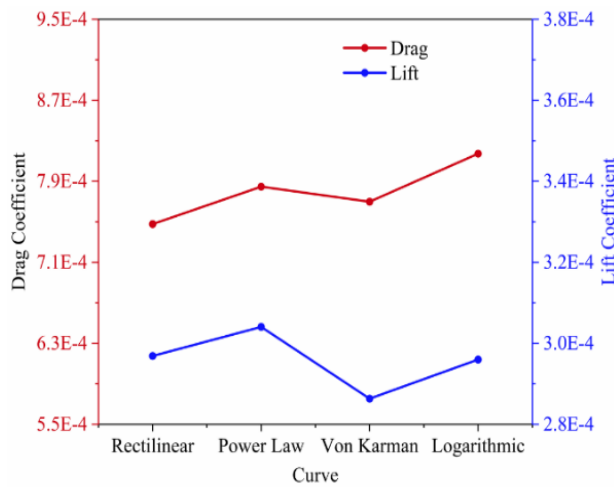
Figure 11 shows the simulation values of the lift and drag coefficients of warheads described by different curves for different angles of attack. The optimal power exponent differs for the logarithmic and power law curves due to different attack angles. Therefore, the logarithmic and power law curves are selected to determine the optimal power exponent. The optimal power exponent n for the warheads described by the power law and logarithmic curves were compared for different angles of attack. The optimal n is 0.65 for the power law curve and 1.3 for the logarithmic curve at a 0° angle of attack. The optimal n is 1 for the logarithmic curve and 0.6 for the power law curve at a 30° angle of attack, 1 for the logarithmic curves and 0.65 for the power law curves at a 40° angle of attack.

The simulation results show that when the wind speed is constant and the angle of attach increases, the frontal area of the warhead, the force acting on the warhead, and the drag and lift coefficients increase. At a 0° angle of attack, the lift coefficient of warhead is the largest for the logarithmic curve, followed by the von Karman curve. The drag coefficient exhibits different responses than the lift coefficient. At the same flow velocity, the drag coefficient of the warhead is the largest for the rectilinear curve. The difference in the drag coefficients between the other three curves is small, with an average difference of 2.03%.

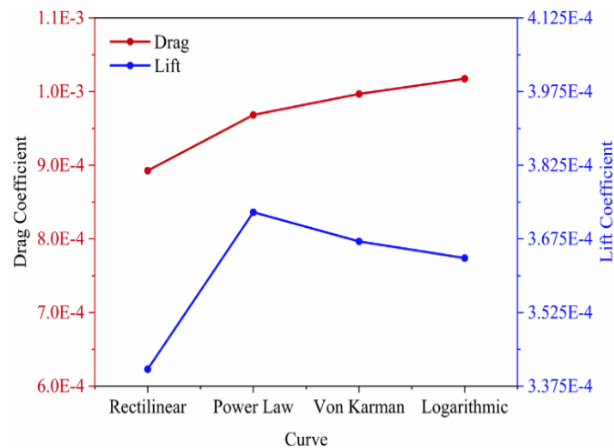
The shape of the warhead, i.e., the slenderness ratio, passivation degree, and inclination angle, are the primary factors affecting the warhead’s resistance (Tang et al. 2010). The passivation degree at the warhead’s tip is the same in this study; thus, the dominant factors affecting the resistance are the slenderness ratio and inclination angle. As the inclination angle increases, the airflow around the warhead and the resistance increase. At a 0° angle of attack, the inclination angle of the bullet with the logarithmic curve cross-section is the smallest, but the arc length of the logarithmic curve is shorter. The larger the slenderness



(a) 0° angle of attack



(b) 30° angle of attack



(c) 40° angle of attack

Fig. 11 Comparison of drag and lift coefficients of warheads described by different curves

ratio of the warhead, the smaller its drag coefficient. The length and slenderness ratio of the bullet are larger for the power law curve and the von Karman curve; therefore, the drag coefficient of the bullet with the power law and the von Karman curves are smaller than that of the logarithmic curve. The larger the number of vertical components of the bullet, the larger the lift coefficient. The larger the

curvature of the warhead with the logarithmic curve, the smaller the angle between the vertical direction and the curve; therefore, the lift coefficient is larger. The warhead with the von Karman curve has the second-largest lift coefficient, followed by the warhead with the power law curve. When the angle of attack is 30°, the warhead with the power law curve has the largest lift coefficient and a relatively small drag coefficient. The difference in the drag coefficient between the warheads with the other three curves is small, but the differences in the lift coefficients differ. The warhead with the von Karman curve has a small lift coefficient, and the difference between the warheads with the rectilinear and logarithmic curves is not large. The lift coefficient of the warhead with the power law curve is the largest at a 40° angle of attack, followed by that with the von Karman curve and that with the logarithmic curve. The drag coefficient of the warhead with the rectilinear curve is the smallest, and that of the warhead with the logarithmic curve is the largest.

The wakes of bullets with different curves are shown in Fig. 12. The comparison of vorticity at different angles is shown in Fig. 13. Due to significant differences in air velocity on both sides of the warhead’s tail, the velocity of the medium near the tail area decreases sharply because of the body’s shielding effect. Therefore, the velocity on both sides of the warhead differs from that at the tail. Inhomogeneous motion occurs in the medium; the air circulates in the rotation direction, creating a vortex. Due to disturbances, the vortex diffuses outward (Li & Xu, 2023; Peng et al., 2023).

Two vortices appear at the tail of all 12 warheads. Their sizes differ because the average velocity is different for different geometric shapes (Bevilaqua & Lykoudis, 1978; Yane & Subaschandar, 2017). The velocity differs on both sides of different curved warheads due to different curvatures, and the velocity difference between the two sides of the projectile body and the tail is different. The velocity and density of the medium affect the tail vortex (Chinnaraj & Sadanandan, 2020). Its size increases with a decrease in the warhead’s arc. When the angle of attack is 0, the difference in the medium’s velocity between the two sides of the warhead is smallest, and the difference in the size of the two symmetric vortices at the tail is relatively small.

The warhead wakes at three attack angles are compared in Fig. 14. When the axis of the warhead has an angle relative to the horizontal direction, the wake has an arch-shaped streamline. At the highest point of the arch, the vertical component of the tail velocity is zero (Abdullah et al., 2022). As the angle of attack grows, the lower surface pressure of the warhead and the stressed area increase.

The forces acting on the warhead at three angles of attack are compared in Fig. 15. The force on the warhead’s tip is the largest at a 0° angle of attack, whereas the force on the tail is relatively small. As the angle of attack grows, the stress area changes from the tip area to the lower part of the warhead, and the stress area increases. The forces on both sides of the warhead increase significantly, and the horizontal and vertical component are increased. The lift and drag forces also increase.

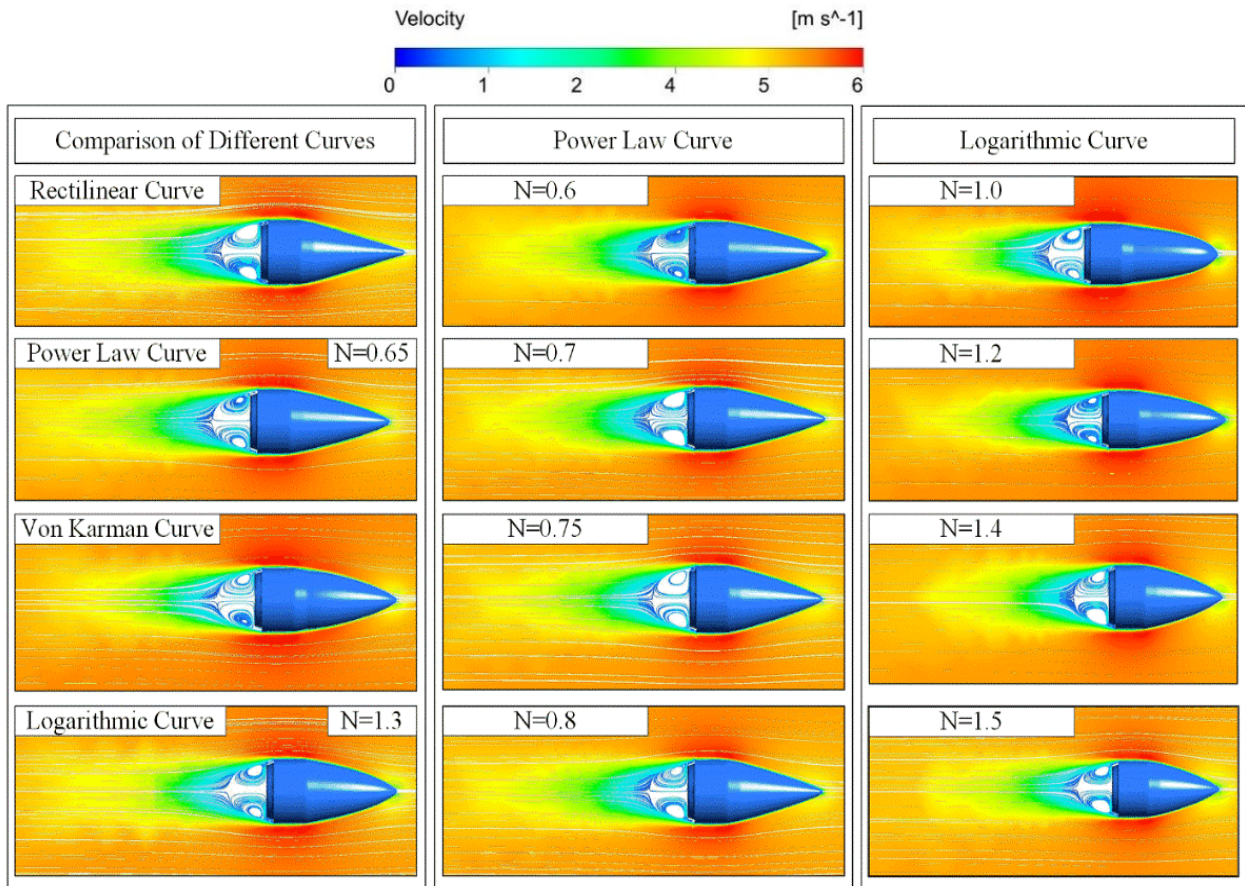


Fig. 12 Comparison of warhead wakes

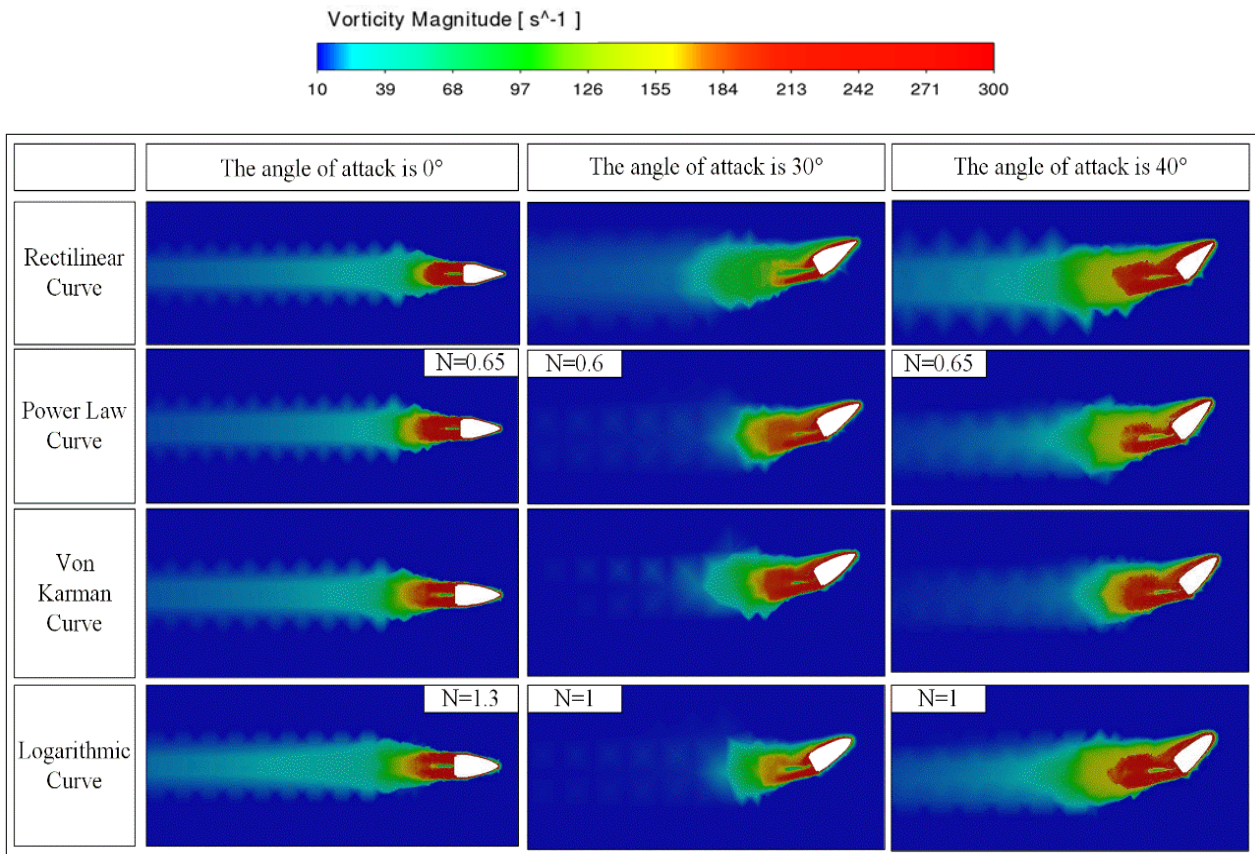


Fig. 13 Comparison of vorticity magnitude

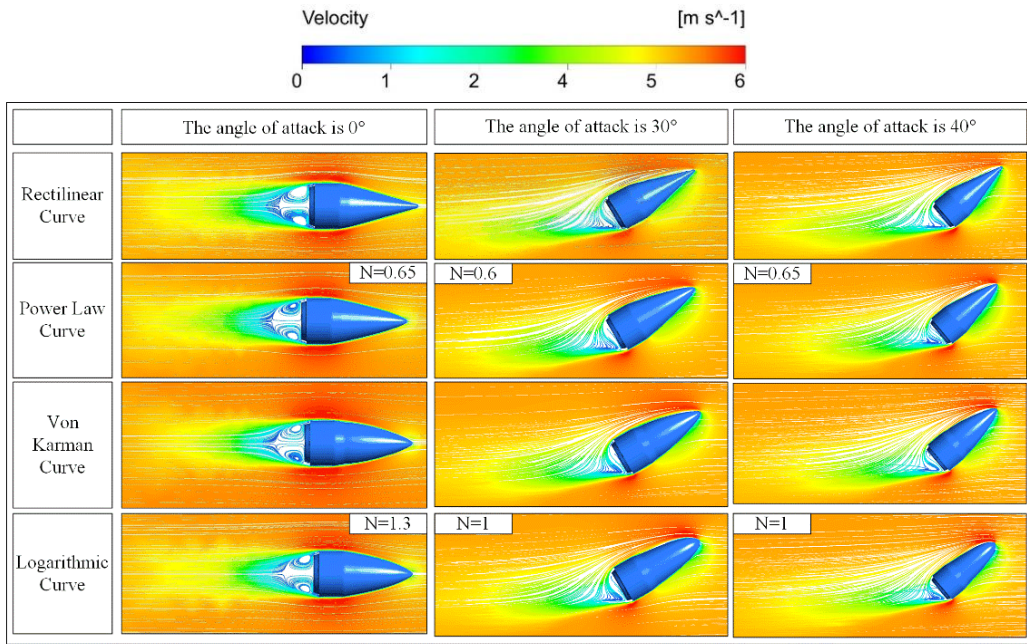


Fig. 14 Warhead wakes at different angles of attack

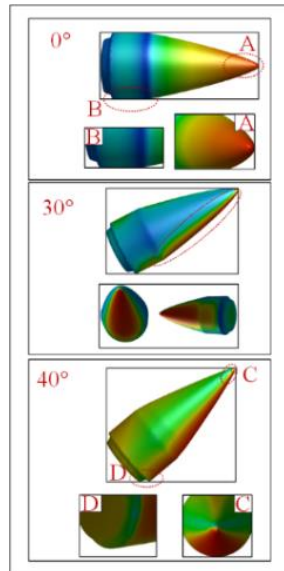


Fig. 15 Forces acting on the warhead

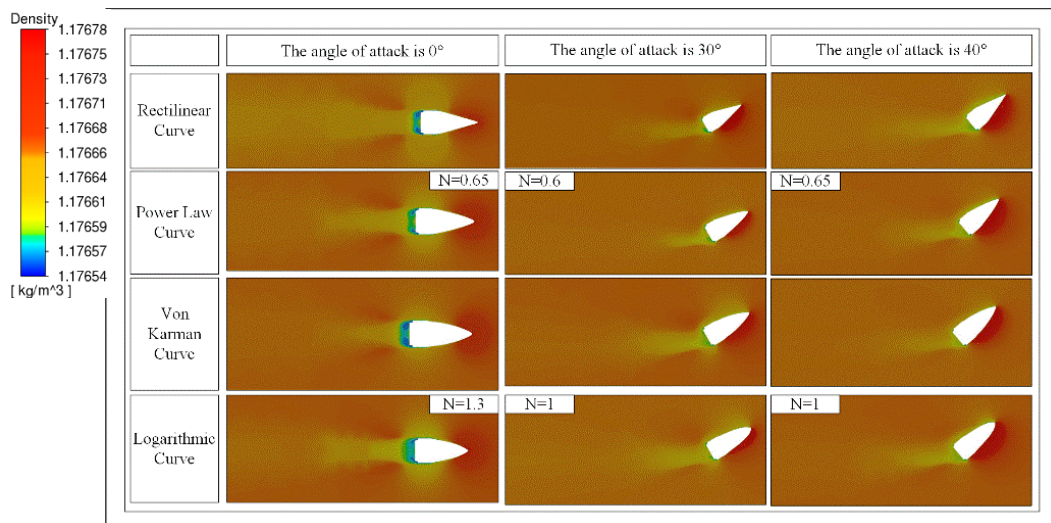


Fig. 16 Comparison of density

Figure 16 shows the density contours of different warheads at different angles. Air density is a measure of the intensity of a gas's movement. The force of the warhead is significantly affected by the gas movement. Therefore, we discuss the changes in the air density near the warhead. As the angle of attack increases, the air density and high density region on the lower side of the warhead increases. Since the arc differs for different warheads, the velocity of the tail is different, resulting in different air densities. The difference in air density between the two sides of the warhead is small at 0° angle of attack.

4. CONCLUSION

We conducted low-speed wind tunnel experiments with warheads with different curves and analyzed their lift and drag coefficients at three angles of attack. The optimal power exponents of the power law and logarithmic curves were determined using computational fluid dynamics simulations. The following conclusions were drawn.

(a) At the same flow velocity, the optimal value of the power exponent differs for different curves due to differences in the angle of attack. The optimal values of the power exponents are 0.65, 0.6, and 0.65 for the power law curve and 1.3, 1, and 1 for the logarithmic curve at 0°, 30°, and 40° angles of attack.

(b) When the angle of attack is 0°, the lift coefficient of the warhead is the largest for the logarithmic curve, followed by the von Karman curve and the power law curve. The drag coefficient of the warhead is the largest for the rectilinear curve. When the angle of attack is 30°, the lift coefficient of the warhead is the largest for the power law curve, followed by the rectilinear and the logarithmic curves. The drag coefficient is the largest for the logarithmic curve, followed by the power law curve, and the von Karman curve in close proximity to the rectilinear curve. At a 40° angle of attack, the warhead with the power law curve has the largest lift coefficient, and that with the rectilinear curve has the smallest one. The warhead with the rectilinear curve has the smallest drag coefficient and that with the logarithmic curve has the largest one.

(c) The bullet curve is as important as the cross-sectional shape. These are critical parameters in aerodynamic design. The curvature affects the bullet's aerodynamic characteristics and must meet the structural layout and volume requirements.

(d) The largest lift coefficients at 0°, 30°, and 40° angles of attack occur for the warhead with the logarithmic curve at a power exponent of 1.3, the warhead with the power law curve at a power index of 0.6, and the warhead with a power law curve at a power index of 0.65.

(e) Choosing an appropriate bullet design is crucial. The proposed warhead with the logarithmic curve has a novel shape. Our results provide new insights into bullet design and aerodynamic properties.

CONFLICT OF INTEREST

The authors declare that they have no known competing financial interests or personal relationships that might influence the work reported in this paper.

AUTHORS CONTRIBUTION

Bo Hao and **Qi Jiang**: Numerical simulation calculations. **Caixian Xu**: Data integration and processing. **Liwei Liu**: Thesis integration.

REFERENCES

- Abdullah, k., Imran, S., Shahid, A., & Muhammad, W. (2022). Numerical and experimental analysis of drag and lift forces on a bullet head. *Aerospace*, 9, 816. <https://doi.org/10.3390/aerospace9120816>
- Bateman, M. J. K., & Force, U. A. (2022). Maximizing Engagement Area Lethality. *Mil. Rev.*
- Bevilaqua, P. M., & Lykoudis, P. S. (1978). Turbulence memory in self-preserving wakes. *Journal of Fluid Mechanics*, 89(3), 589-606. <https://doi.org/10.1017/S002211207800275X>
- Chinnaraj, M., & Sadanandan, R. (2020). The Effect of swirling air-to-liquid momentum ratio on the spray and droplet characteristics. *Journal of Applied Fluid Mechanics*, 13(3), 827-837. <https://doi.org/10.29252/jafm.13.03.30345>
- Davis, B. S., Guidos, B. J., & Harkins, T. E. (2009). Complementary roles of spark range and onboard free-flight measurements for projectile development. *Army Research Laboratory, Weapons and Materials Research Directorate, ARL.*
- Doig, G., Barber, T. J., Leonardi, E., Neely, A. J., & Kleine, H. (2010). Aerodynamics of a supersonic projectile in proximity to a solid surface. *AIAA*, 48(12), 2916-30. <https://doi.org/10.2514/1.J050505>
- Li, L. C., & Xu, B. (2023). Numerical simulation of hydrodynamics characteristics in a tank with an up-down reciprocating agitator. *Journal of Applied Fluid Mechanics*, 16(7), 1455-1466. <https://doi.org/10.47176/jafm.16.07.1721>
- Ma, J., Chen, Z. H., Huang, Z. G., Gao, J. G., & Zhao, Q. (2016). Investigation on the flow control of micro-vanes on a supersonic spinning projectile. *Def Technol*, 12(3), 227-33. <https://doi.org/10.1016/j.dt.2016.01.008>
- McCoy, R. (1999). *Modern exterior ballistics: the launch and flight dynamics of symmetric projectiles*. Atlgen, PA: Schiffer Publishing Ltd.
- Peng, F., Yan, F., & Liang, J. N. (2023). Experimental study on wake characteristics of secondary grooved cylinders with different depths. *Journal of Applied Fluid Mechanics*, 16(5), 1057-1073. <https://doi.org/10.47176/JAFM.16.05.1592>

- Qian, Z. D., Hu, X. Q., Huai, W. X., & Amador, A. (2009). Numerical simulation and analysis of water flow over stepped spillways. *Science in China Series E: Technological Sciences*, 52, 1958-1965. <https://doi.org/10.1007/s11431-009-0127-z>
- Rahman, M. R. (2020). Computational analysis of aerodynamic parameters for supersonic artillery projectiles. *International Journal of Mechanical Engineering*, 6, 1-18. <https://doi.org/10.53555/mce.v6i8.3832>
- Rhee, P. M, Moore, E. E., Joseph, B., Tang, A., Pandit, V., & Vercruyse, G. (2016). Gunshot wounds: A review of ballistics, bullets, weapons, and myths. *Trauma Acute Care Surg*, 80, 853-867. <https://doi.org/10.1097/TA.0000000000001037>
- Sadowski, L. M., Malatesta, E. T., & Huerta, J. (1984). 30-mm tubular projectile. *Tech. Rep: U.S. Army armament research and development center, fire control and small caliber weapon systems laboratory*.
- Shi, J. G., Yi, W. J., & Guan, J. (2017). Identification of projectile drag coefficient based on particle swarm-Newton algorithm. *Journal of Weapons and Equipment Engineering*, 38(2), 23-26. <https://doi.org/10.11809/scbgxb2017.02.006>
- Shih, T. H., Liou, W. W., Shabbir, A., Yang, Z. G., & Zhu, J. (1995). A new k- ϵ eddy viscosity model for high Reynolds number turbulent flows. *Comput Fluids*, 24(3), 227-238. [https://doi.org/10.1016/0045-7930\(94\)00032-T](https://doi.org/10.1016/0045-7930(94)00032-T)
- Shinde, P., Ohol, S. S., & Tripathi, V. K. (2023). Shape optimization of an asymmetric airfoil for low wind speed region having adjoint-based optimization technique. *Journal of Applied Fluid Mechanics*, 16(2), 299-310. <https://doi.org/10.47176/jafm.16.02.1426>
- Silton, S. I. (2005). Navier-Stokes computations for a spinning projectile from subsonic to supersonic speeds. *Spacecraft Rockets*, 42(2), 223-31. <https://doi.org/10.2514/1.4175>
- Silton, S. I., & Weinacht, P. (2008). *Effect of rifling grooves on the performance of small caliber ammunition*. Tech. Rep. MD: U.S. Army Research Laboratory.
- Silva, U. S., Sandoval, J. M., Flores, L. A., Munoz, N., & Hernandez, V. (2011). Numerical simulation and experimental study of flowfield around a bullet with a partial core. *Journal of Applied Mechanics*, 78(5), 051020. <https://doi.org/10.1115/1.4004297>
- Tang, W. D., Jiang, W., Gui, W. Y., & Zhang, R. W. (2010). Study on the selection of busbar line type for the head of a rotating missile. *Acta Aerodynamica Sinica*, 38(2), 23-26.
- Yane, T., & Subaschandar, N. (2017). Behavior of mean velocity in the turbulent axisymmetric outer near wake. *Journal of Applied Fluid Mechanics*, 10(6), 1629-1636. <https://doi.org/10.29252/JAFM.73.245.27826>